# MIT Libraries | DSpace@MIT

## MIT Open Access Articles

## *Three-Dimensional Synthetic Aperture Imaging and Resolution of Multi-Phase Flows*

**Massachusetts Institute of Technology**

# AJK2011-11011

# THREE-DIMENSIONAL SYNTHETIC APERTURE IMAGING AND RESOLUTION OF MULTI-PHASE FLOWS

**Jesse Belden** *
Massachusetts Institute of Technology
Department of Mechanical Engineering
Cambridge, MA 02139, USA
Email: jbelden@mit.edu

**Sai Ravela**
Massachusetts Institute of Technology
Department of Earth, Atmospheric and Planetary Sciences
Cambridge, MA 02139, USA
Email: sairavela@gmail.com

**Tadd T. Truscott**
Brigham Young University
Department of Mechanical Engineering
Provo, UT 84602, USA
Email: truscott@byu.edu

**Alexandra H. Techet**
Massachusetts Institute of Technology
Department of Mechanical Engineering
Cambridge, MA 02139, USA
Email: ahtechet@mit.edu

## ABSTRACT

Three-dimensional multiphase fluid flows demand advanced and innovative measurement systems in order to fully resolve the flow physics. Dense bubbly multiphase flows cannot be readily imaged by traditional, non-invasive flow measurement techniques due to the bubbles occluding optical access to the interior regions of the volume of interest. We present a novel technique for imaging these flows, which allows for determination of the 3D bubble distribution and bubble sizes despite the imaging challenges. By using synthetic aperture (SA) refocusing we are able to reparameterize images captured by an array of cameras to reconstruct a 3D volumetric map of the bubble field for every time instance. The SA refocusing technique has the unique ability, over conventional imaging methods, to see-through partial occlusions in the scene due to the configuration of the camera array and reconstruction algorithms, making it an ideal tool for resolving multiphase flows. Relatively dense bubbly flows can be resolved with good accuracy. We present fundamentals of the synthetic aperture methodology, a feature detection algorithm for extracting bubble size and location, and results from application of the technique to a bubble-entraining plunging jet.

## 1  INTRODUCTION

Bubbly flows are ubiquitous in a variety of engineering problems ranging from air-sea interaction to ship surface signature from wave breaking to propellor cavitation to industrial processes. However, measurement of problems of this class presents several challenges. Often, interesting flows are optically dense due to large void fractions which limits applicability of several techniques. Full temporal and three-dimensional spatial resolution of the bubble fields is a desirable outcome of measurement, but further limits the class of available instruments. Conductivity probes offer a proven method for measuring void fraction and bubble count rate, but only do so locally and are invasive [1]. Acoustic measurements using hydrophones can provide overall void fraction and bubble count, as well as bubble size spectra [1], but cannot provide detailed information about the location or track of bubbles within a flow. Other authors used planar shadow imaging to resolve bubble size and location in two dimensions. [2]. To obtain information about the location and track of bubbles in three-dimensions as well as size, three-dimensional imaging techniques are often the tool of choice. Pereira et al. [3] applied defocusing digital particle image velocimetry to measure bubble fields, although the bubble sizes were relatively small.

---

*Address all correspondence to this author.

Tian et al. [4] used digital holography to measure bubble size and location with a very efficient algorithm allowing for near real-time output. However, the digital holographic approach is typically limited to lower void fractions or flows that are not too optically dense.

In this paper, we discuss a technique based on synthetic aperture (SA) imaging that enables instantaneous resolution of three-dimensional bubble fields. The fields can be quite dense because SA imaging allows for reconstruction despite partial occlusions. To generate a flow field with variable bubble density and size, we employed the classic experiment of a liquid jet impinging on on a free surface. Early studies of liquid jets impinging on the free surface of the same liquid by Lin and Donnelly [5] identified two regimes of importance: when the jet is laminar or turbulent. A comprehensive table showing the different regimes studied by different groups is presented by Chanson [1]. The laminar case is characterized by a large deformation of the free surface (cylindrical like) which does not entrain air until a critical Weber number where the jet radius and velocity exceeds a critical value [6–9]; the deformed surface can descend several jet diameters under the surface before forming bubbles. The turbulent case is characterized by an instability that forms in the jet before it impinges on the free surface and bubbles are formed just below the free surface as air is trapped by the fast moving wave like instability. Several studies have observed this phenomenon and studied it directly [5, 6, 10] or used it to develop methods for measuring bubbly flows [1, 11].

The phenomenon is an excellent candidate for determining the ability of a system to resolve multi-phase flow fields. It is simple to set-up, easy to scale by simply changing the jet diameter or speed, and a quasi-steady state plume can be formed in just a few seconds. For these reasons we have utilized a turbulent air entrainment setup to perform measurements of a multi-phase flow field using the synthetic aperture imaging technique.

## 2  EXPERIMENTAL METHODS

To generate a steady-state jet, an outlet tube and nozzle was mounted below a tank with constant head height of water, as shown in Fig. 1. The tube and nozzle inner diameter could be set at either 6.35, 9.53 or 12.7 mm. All data presented in this paper comes from the 6.35 mm nozzle setup with the nozzle exit 21 mm above the free-surface ($h = 21$ mm). A bilge pump cycled water from the test tank to the head tank at a flow rate equal to the flow rate through the nozzle. As a fail-safe to ensure maintenance of a constant head pressure, an overflow outlet and tank was untilized. The head and overflow tanks, outlet tube and nozzle were all mounted to a vertically arranged precision traverse to allow the nozzle height (and thus just impact velocity) to be varied without changing the overall pressure drop between the head tank and the nozzle outlet.

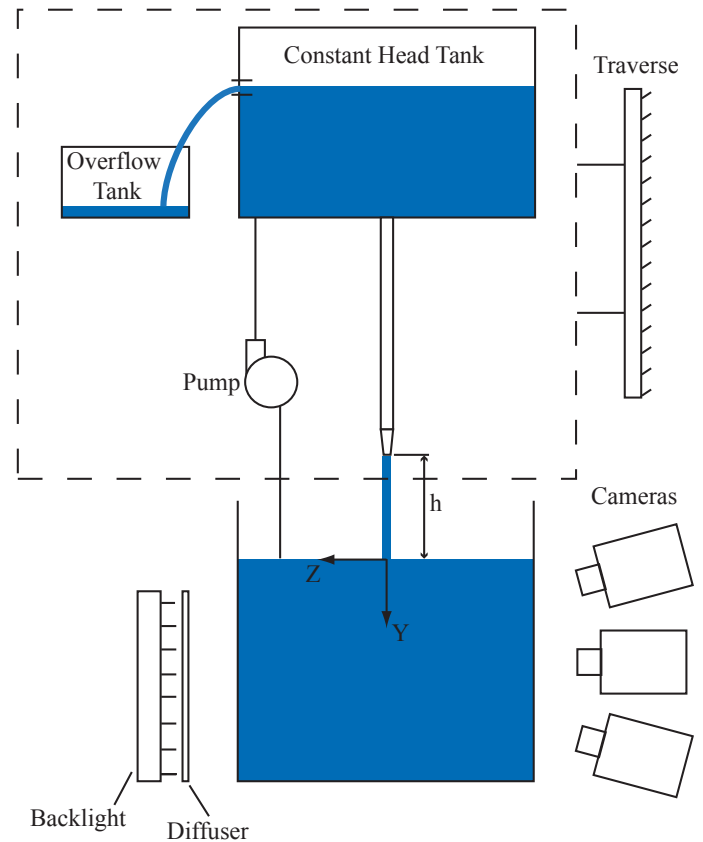Nine high speed Photron Fastcam cameras (two model SA1,



**FIGURE 1**: EXPERIMENTAL SETUP FOR BUBBLE ENTRAINING FREE-SURFACE PIERCING JET.

four model SA3, three model SA5) arranged in a $3 \times 3$ array imaged the flow (Fig. 2). The cameras were mounted on a custom 80/20® frame which allowed the cameras to be angled and thus the field of view (FOV) of each camera to be overlapped. All cameras were equipped with Nikon Nikkor 50 mm lenses set to f/8 in order to keep the entire volume of interest in focus; this is a pre-requisite for the synthetic aperture refocusing [12]. Cameras were synced to a master camera and each acquired 1024 pixel × 1024 pixel, 12-bit images (later saved as 8-bit tiff images) at a rate of 1000 frames per second (fps). A white backlight and diffuser provided illumination for the flow. Backlighting causes the edges of bubbles to appear dark against the white background [2, 13]. Setting the exposure time to 0.1 ms (10% of the total frame length) afforded enough light without causing bubbles to streak within the image (due to over exposure). A sample image from the central camera of the array (pre-processed for contrast enhancement) is shown in Fig. 3.
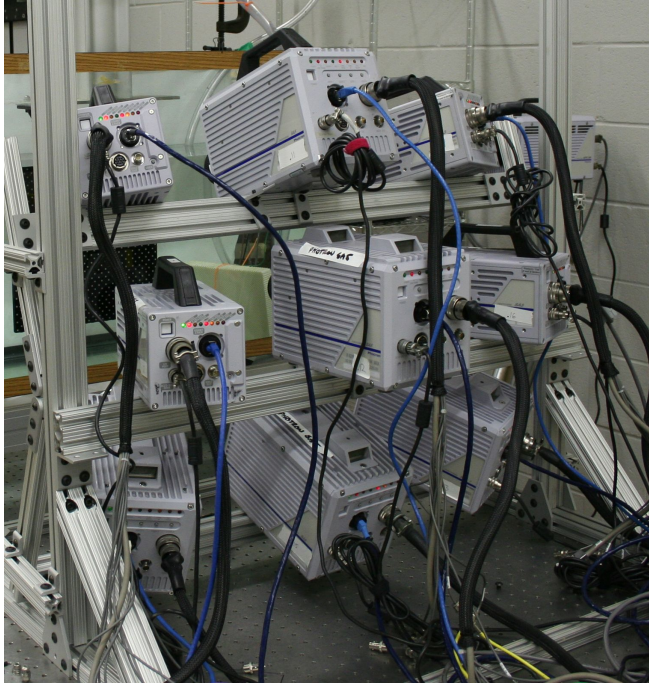
2

**FIGURE 2**: ARRANGEMENT OF NINE HIGH SPEED PHOTRON CAMERAS ON A CUSTOM 80/20® FRAME.
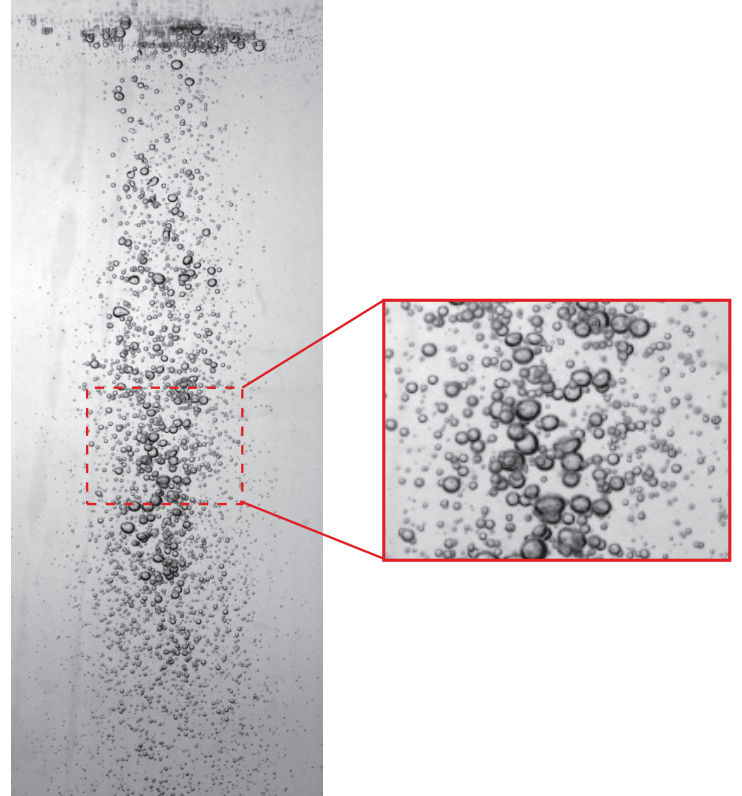


**FIGURE 3**: SAMPLE PRE-PROCESSED IMAGE FROM THE CENTRAL CAMERA OF THE ARRAY FROM THE 6.25 mm NOZZLE TEST AT HEIGHT 21 mm.

# 3 SYNTHETIC APERTURE IMAGING

Synthetic aperture imaging is a subset of light field imaging, which captures as many light rays emanating from a scene as possible [14, 15]. Synthetic aperture refocusing is a post-capture algorithm that reprojects in-focus images from multiple cameras onto planes in the imaged scene and recombines the images to create refocused images; objects that lie on these focal planes appear sharp while objects not on this plane appear blurred [14, 15]. The application of synthetic aperture refocusing to three-dimensional particle image velocimetry (3D SAPIV) was described thoroughly in our previous work [12], and many of the same principles apply here. In general, the first step in SA refocusing involves establishing mapping functions between the camera image planes and world coordinates,

$$\mathbf{u}_j^i = F\left(\mathbf{X}_j ; p^i\right) \tag{1}$$

where $\mathbf{u}_j$ is the 2x1 vector of the $j^{th}$ image point coordinates, $[u_j, v_j]^T$, $X_j$ is the 3x1 vector of the $j^{th}$ world point coordinates, $[X_j, Y_j, Z_j]^T$, $p^i$ is a set of parameters defining the model of the $i^{th}$ camera and $F$ defines the form of the model. Using this model, each image from $N$ cameras are reprojected onto $k$ focal planes. The reprojected image from the $i^{th}$ camera onto the $k^{th}$ focal plane will be referred to as $I_{FP_{ki}}$. In [12], the refocused images were generated by taking the arithmetic mean,

$$I_{SA_k} = \frac{1}{N} \sum_{i=1}^{N} I_{FP_{ki}} \tag{2}$$

In Tomographic PIV [16], reprojected rays are multiplied together to enhance the signal-to-noise ratio. However, if any camera has an occluded view of an object (i.e., zero or a very small value for a pixel), multiplication brings the entire reprojected voxel to zero. Instead of using Equation 2, the signal-to-noise ratio can be improved by refocusing the images according to

$$I_{SA_k} = \prod_{i=1}^{N} \left(I_{FP_{ki}}\right)^n \tag{3}$$

3

Copyright © 2011 by ASME

as suggested by [17], where $n$ is an exponent between 0 and 1. This allows for enhancement of the signal-to-noise ratio without letting any camera with an occluded view of an object to prevent that object from being refocused, because a small number raised to an exponent between 0 and 1 is non zero. Equation 3 was applied to all data in this paper using $n = 1/3$.

Many options exist for the specific form of $F$, and the parameters are normally found via a calibration procedure. In the present paper, a precision machined calibration plate traversed through the target volume with $Z$ location increments of 5 mm provided calibration targets. The average calibration in pixels/mm from the center camera image of the plate at the $Z$ location farthest from the cameras was used to convert the reference geometry of the calibration plate from mm to pixels (herein, 4.1 pixels/mm). Second-order polynomial fits served as the mapping functions between image coordinates and reference coordinates on each $Z$ calibration plane, and linear interpolation was used to find the polynomial fits on $Z$ planes between each calibration plane, as has been used in [12, 18, 19]. The spacing between focal planes was set to 0.2 mm, which was chosen to be large enough such that adjacent planes were not redundant. For more information on focal plane spacing, see [12].

Refocused images at depths -10, 0 and 10 mm are shown in Fig. 4 for a single time step from the 6.25 mm nozzle test at height 21 mm. All images were preprocessed to enhance contrast prior to application of the refocusing algorithm. The red circles on each image highlight locations where a certain bubble is in focus on one depth plane, but blurred from view on other depth planes.

## 4 FEATURE EXTRACTION

It is evident that SA refocusing is a powerful technique for isolating the depth location and in-plane features of bubbles in a dense flow, but the features must be extracted from the focal stack in order to quantify certain parameters. In this study, we are interested in measuring the bubble sizes and three-dimensional locations. The steps of the proposed algorithm for feature extraction are listed below, and each is explained in further detail thereafter:

1. Apply attenuation function to suppress noise and make refocused images good candidates for feature extraction.
2. Generate minimum images over depth windows and store corresponding depth maps.
3. Generate edge map of minimum images and label possible features.
4. Apply either ellipse detection (for "large" bubbles) or grayscale threshold (for "small" bubbles).
5. Validate resulting bubbles.

The **first step** in the algorithm involves making the focal stack images better candidates for feature extraction; namely, by

reducing the amount of out of focus noise and leaving the sharply refocused bubbles. Here, we aim to construct a noise attenuation function that suppresses noise and rewards regions with large gradients, which are often associated with bubble edges. First, a metric is computed for each depth layer of the refocused volume. The metric gives a single value for each depth layer and is therefore calculated on a windowed version of the refocused volume to emphasize local features. For the data presented here, the window size is $l \times l \times n_Z$ voxels, where $l$ is a length scale chosen to be 8 voxels in the present study and $n_Z$ is the depth dimension of the entire refocused volume in voxel units. First, the windowed volume ($I_o$, assumed to be grayscale) is normalized,

$$I(i,j,k) = \frac{I_o(i,j,k) - \bar{I}_o}{\sigma(I_o)} \tag{4}$$

For each depth layer of the windowed volume, the in-plane gradient is calculated by,

$$\mathbf{g}(i,j,d) = \nabla I(i,j,d) = \left( \frac{\partial I(i,j,d)}{\partial x}, \frac{\partial I(i,j,d)}{\partial y} \right) \tag{5}$$

where $I(i,j,d)$ is the normalized intensity at index $(i,j)$ in the $d^{th}$ depth layer. The proposed metric is defined as

$$H(d) = \sum_{i,j} f(\mathbf{g}(i,j,d)) exp\left[ \frac{f(\mathbf{g}(i,j,d))}{2(\sigma')^2} \right] \tag{6}$$

where $\sigma' = 1/\sigma$ and $\sigma$ is the standard deviation of the windowed normalized refocused volume and $f$ is a "gradient feature" coming from a set of possible gradient features: $f \in \{ |g_x|, |g_y|, \sqrt{\mathbf{g}^t \mathbf{g}} \}$. Similarly, higher order derivatives are also possible, but we restrict ourselves to the first order in this work. Namely, the absolute value of the components of the gradient are used to define

$$E_x(d) = \sum_{i,j} |g_x(i,j,d)| exp\left[ \frac{|g_x(i,j,d)|}{2(\sigma')^2} \right] \tag{7}$$

where $g_x$ is the x component of the gradient; $E_y$ is calculated in a similar manner. Clearly, large values of gradient magnitude result in large values of $E_x$ and $E_y$. The final metric is calculated as the maximum of the metric applied to x-direction data and y-
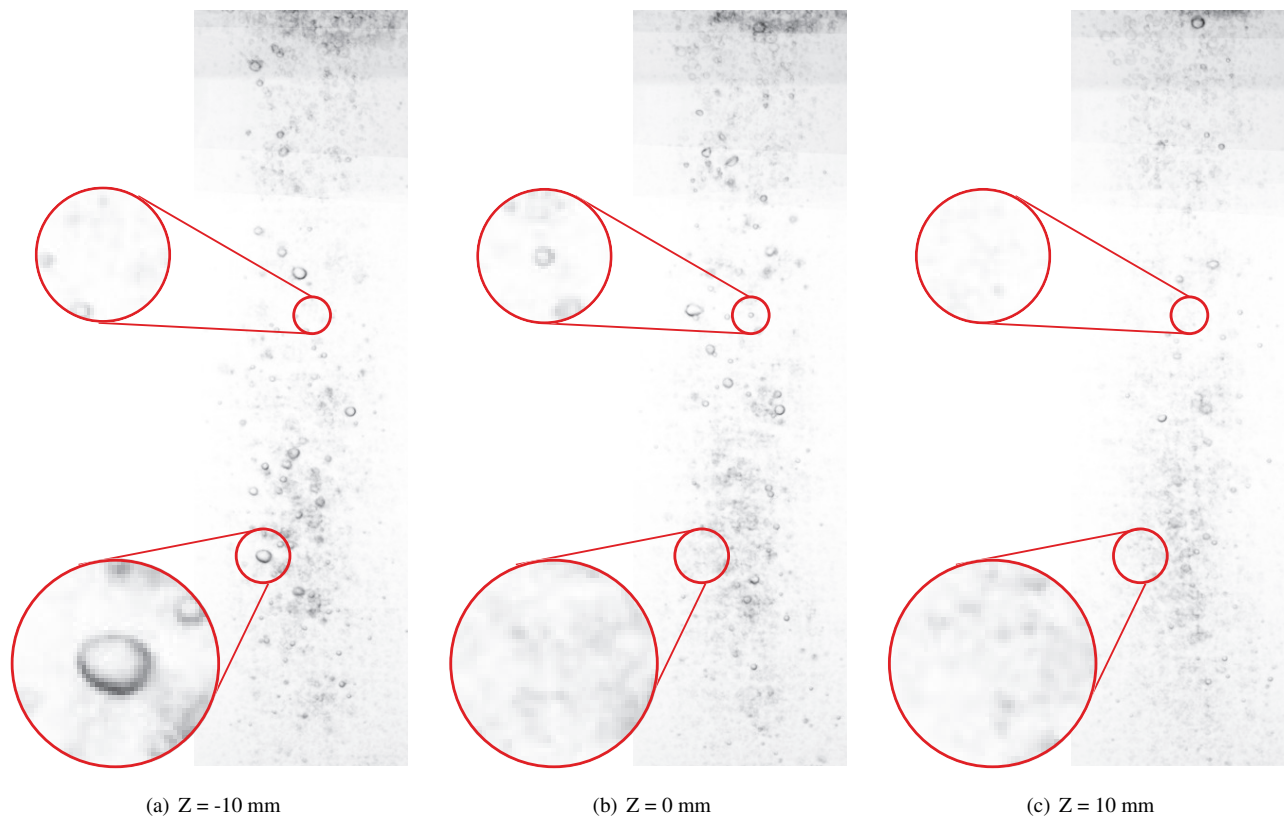
4

**FIGURE 4**: SYNTHETIC APERTURE REFOCUSED IMAGES AT (a) Z = -10 mm, (b) Z = 0 mm AND (c) Z = 10 mm. THE RED CIRCLES ON EACH IMAGE HIGHLIGHT LOCATIONS WHERE A CERTAIN BUBBLE IS IN FOCUS ON ONE DEPTH PLANE, BUT BLURRED FROM VIEW ON OTHER DEPTH PLANES.

direction data, $E(d) = \max\left(E_x(d), E_y(d)\right)$, for each depth. The metric is calculated in windows covering the entire volume; no window overlap is used in the present study. Because the metric is a summation of functions of the local gradient, it rewards *regions* with large gradients; for example, the edges of bubbles. Therefore, the length scale, $l$, should be chosen such that portions of bubbles are within the window rather than a single edge pixel, for example. However, making the length scale too large will retain unwanted information, and thus the choice of $l$ is somewhat experimental.

Figure 5 shows $E$ as a function of depth for one window of the bubble volume. Slices from the original refocused volume at three depths are shown on the graph. The first image corresponds to the largest peak, and as can be seen a bubble is contained within the window. The second image contains a smaller bubble that has less well defined edges. This bubble does cause a spike in $E$, but the peak is not as large because the gradients are not as strong. Finally, the third windowed image is more representative of the background noise, and does not increase $E$ much

over the background level.

The question still remains: what form should the attenuation function take? Here, we use the discrete cumulative distribution function (cdf) of $E$, which naturally assigns low levels a value near zero and high levels a value near one. The cdf values corresponding to each calculated $E$ are assembled into a matrix; the nodes of the matrix are at the in-plane centers of the windows at each depth layer. Finally, the cdf matrix is interpolated onto a matrix of equal size to the refocused volume and the interpolated matrix is multiplied point-by-point by the refocused volume.

The **second step** of the algorithm involves isolating the focus plane of the bubbles. Rather than applying a focus metric to every refocused image, a "minimum" image is calculated over a depth window, similar to other previous works [4]. Many metrics exist for defining the minimum image (e.g., gradients, entropy), but because the bubbles edges are defined by local minima in intensity, the intensity value itself serves as the metric in this study. At each pixel, the minimum intensity value is found over the depth of a stack of refocused images and the depth corre-
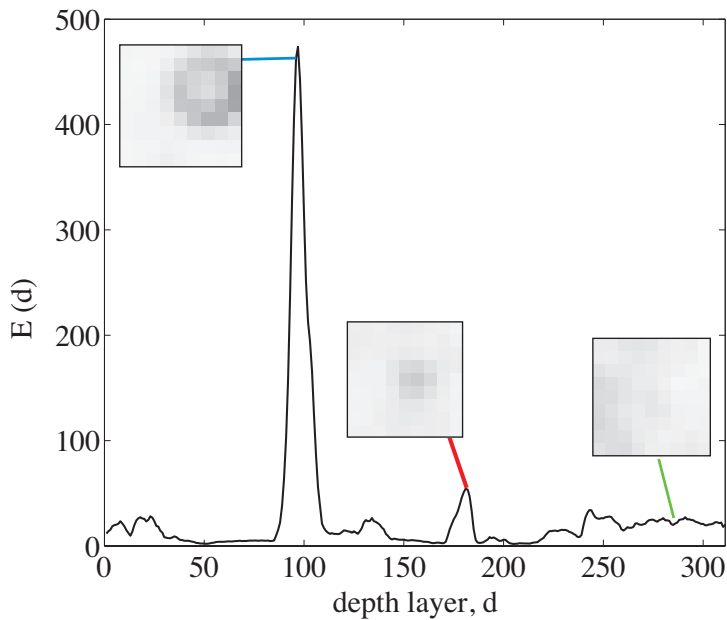
5

Copyright © 2011 by ASME

**FIGURE 5**: *E* AS A FUNCTION OF DEPTH FOR ONE WINDOW OF THE BUBBLE VOLUME. SLICES CORRESPONDING TO PEAKS ARE SHOWN.

sponding to each minima is recorded into a depth map. Other authors (e.g. [4]) have used this approach over the entire focal stack for lower density flows, but the larger bubble density in the present study would lead to many overlapping bubbles in the minimum image. Therefore, the focal stack is windowed to yield stacks of smaller depth, and a minimum image and depth map is generated for each window. Herein, a window size of 50 voxels yielded minimum images with relatively few instances of bubble overlap, but also was large enough to contain the depth of focus of even large bubbles. Sample portions of minimum images are shown in Fig. 6; Fig. 6(a) is a minimum image generated from the original refocused volume and Fig. 6(b) is generated from focal planes processed by the attenuation procedure.

Labeling potential features on the minimum images constitutes the **third step** of the algorithm. A Sobel edge detector operates on the minimum images to define edges, which are subsequently labeled using an algorithm based on connectivity of neighboring pixels. This results in segmented portions of the minimum image corresponding to different bubbles, although bubbles very near to each other may get grouped into a single feature. Any feature described by three or less pixels is removed; this removes noise, but also some potential small bubbles. In the future, more robust noise rejection will be implemented.

In the **fourth step** of the algorithm, geometric properties of the bubbles are extracted from the labeled features. As discussed in [20] for backlighting of bubbles with an incoherent source, if bubbles are large enough, the edges will appear dark and a bright
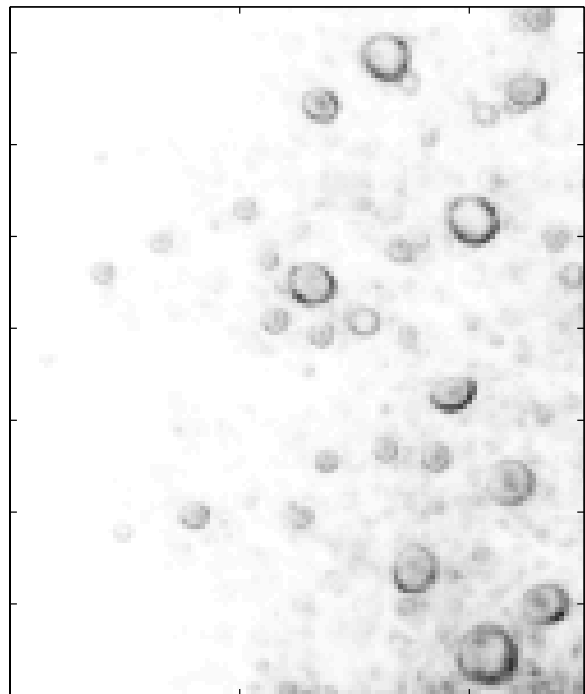


(a)
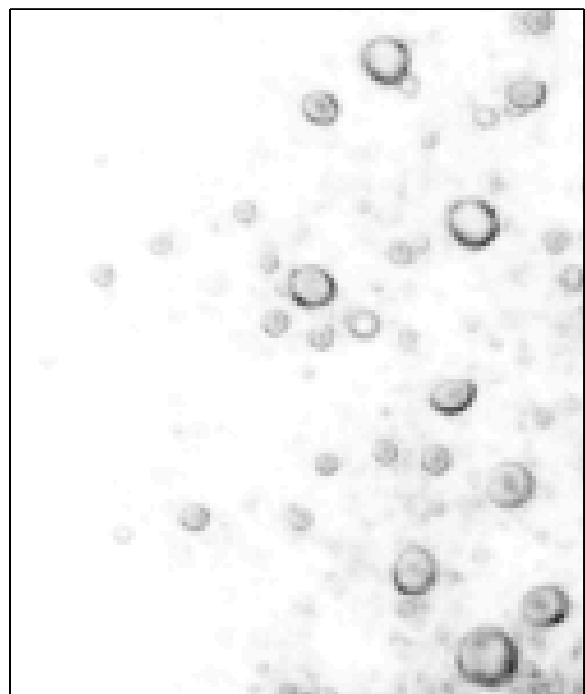


(b)

**FIGURE 6**: MINIMUM IMAGE USING THE ORIGINAL REFOCUSED VOLUME (a), AND MINIMUM IMAGE AFTER APPLICATION OF THE ENTROPY ATTENUATION FUNCTION (b).
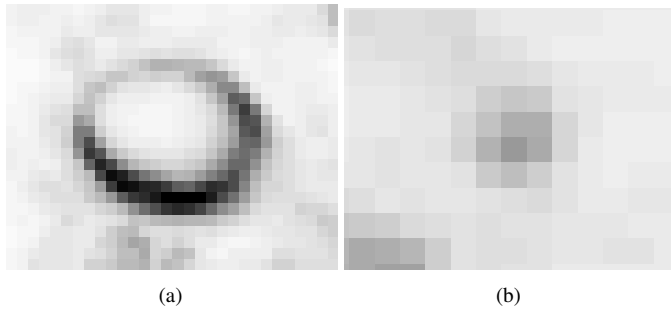
6

**FIGURE 7**: EXAMPLE OF A LARGE BUBBLE WITH WELL DEFINED EDGE (a), AND SMALL BUBBLE WITH LESS EDGE DEFINITION (b).

spot appears in the middle, but for smaller bubbles the middle bright spot is less evident and only dark edge pixels appear. This effect carries through to the minimum images generated from SA refocusing. Figure 7(a) shows a "large" bubble from a minimum image with well defined edge pixels and a bright center, while Fig. 7(b) shows a "small" bubble which consists only of dark edge pixels. To extract size and location from large bubbles, a Hough transform or similar edge pixel voting scheme offers a good solution. In this study, because larger bubbles are often not spherical, the ellipse detection scheme described by [21] is applied. To determine ellipse parameters with higher accuracy, the vote weighted average of the parameter value with the highest votes and the parameter values on either side is taken for each parameter. This approach is not suitable for small bubbles that lack sufficient edge definition. For each small bubble, a local region is thresholded using the mean grayscale value (similar to [20]), to generate a binary image with zeros defining the bubble and ones defining the background. The centroid and equivalent diameter formed by the dark pixels are calculated from the binary image. To distinguish between large and small bubbles in this study, the equivalent diameter of each feature from the initial labeling is calculated and any feature with diameter less than four pixels is considered to be a small bubble.

As a **fifth step** to the algorithm, any detected bubble with center coordinates within a larger bubble is considered to be noise and is removed. Further validation to remove noise detected as bubbles and to properly identify overlapping bubbles is the subject of ongoing work.

The contours of bubbles detected on the same portion of the minimum image as shown in Fig. 6(b) are drawn in red in Fig. 8. Clearly, there is a high rate of success in bubble detection. In more dense and noisy areas of the minimum images, the instances of noise detected as bubbles and missed detection of overlapping bubbles increases, but overall the results are very promising. For each detected bubble, values from the depth map inside the bubble contour and within one pixel distance of the
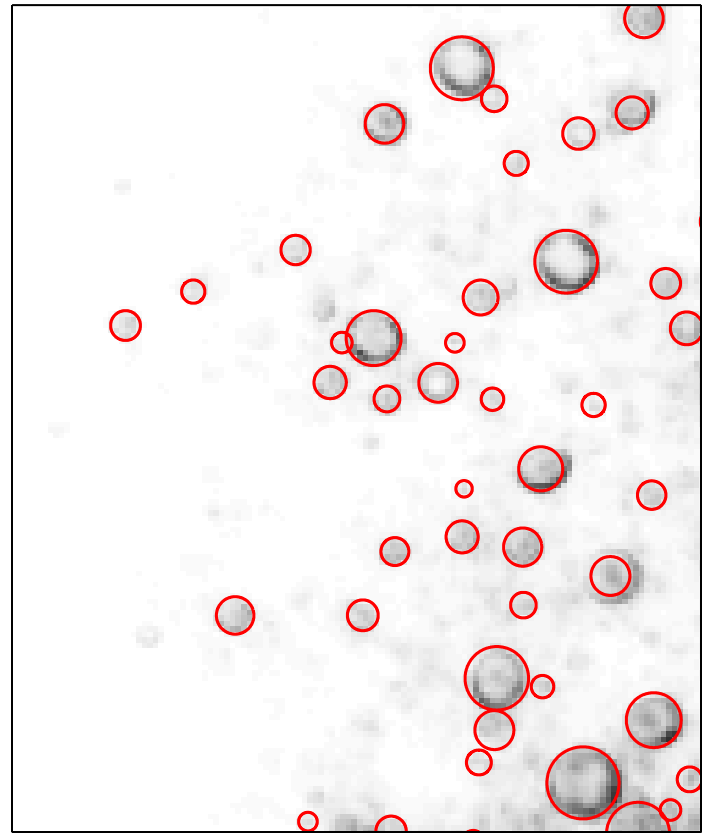


**FIGURE 8**: RESULT OF THE BUBBLE FEATURE EXTRACTION ALGORITHM. BUBBLE CONTOURS ARE OVERPLOTTED ON THE SAME PORTION OF THE MINIMUM IMAGE SHOWN IN FIGURE 6(b).

contour are used to define the depth location of the bubble. The depth is calculated as the weighted mean of contributing pixels from the depth map. Conservatively, the resolution of the depth location is $\pm$ 0.1 mm (half the focal plane spacing), but the resolution is likely even better due to the weighted average.

## 5  RESULTS AND DISCUSSION

The SA refocusing and bubble detection algorithm were applied to one time step of data from the 6.35 mm nozzle setup with the nozzle exit 21 mm above the free-surface to yield instantaneous bubble size and location information. The distribution of the calculated minor and major axes of the ellipses describing the bubbles are shown in Fig. 9(a) and 9(b), respectively. The small bubbles are assumed to be spherical, and thus the minor and major axis of a small bubble is equal to the radius. The range of $a$ and $b$ is 0.34 mm to 1.99 mm. The low end of the range corresponds to the smallest labeled features retained for processing (feature defined by three or less pixels were removed) and thus

7
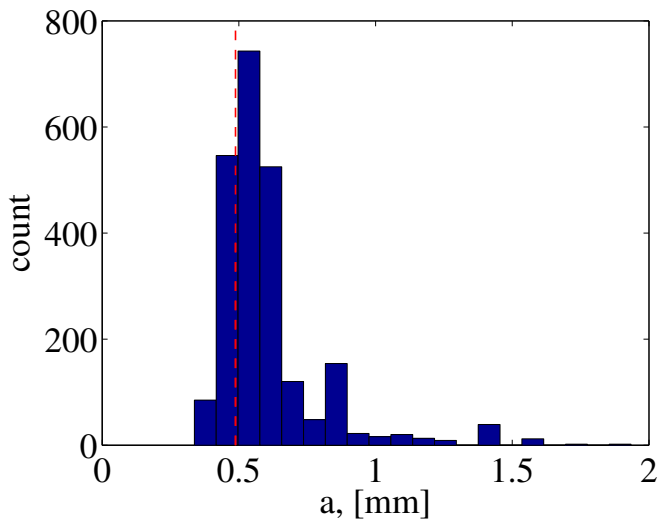
(a) Distribution of major axes
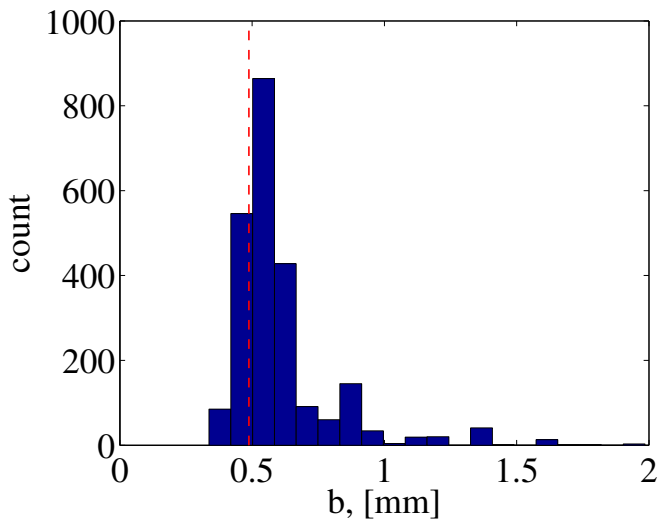


(b) Distribution of minor axes

**FIGURE 9**: DISTRIBUTION OF THE CALCULATED MAJOR AXES (a), AND MINOR AXES (b) OF THE BUBBLES. VALUES TO THE LEFT OF THE DASHED RED LINES CORRESPOND TO "SMALL" BUBBLES AND TO THE RIGHT CORRESPOND TO "LARGE" BUBBLES.

represents the low end limit on resolution for this implementation of the algorithm. The dashed red lines on each plot mark the value below which bubbles are considered "small" with respect to the processing.

The distributions reflect the expectation that more small bubbles remain in the volume than large bubbles due to buoyancy.

The plot of three-dimensional spatial location and size of the bubbles in the flow field shown in Fig. 10 yields further insight. Marker sizes are scaled by the bubble diameter, which is calculated as the average of the minor and major axes for the large bubbles. As can be seen, the large bubbles present in the flow reside close to the axis of the nozzle where high momentum fluid entrains the bubbles. Buoyancy prevents the larger bubbles from penetrating as deep as the small bubbles. Smaller bubbles are more uniformly distributed throughout the flow and penetrate deeper. At a certain depth, the influence of the jet momentum reduces and buoyancy causes the small bubbles to rise along the outer periphery of the volume.

## 6 CONCLUSIONS

The pervasiveness of bubbly flows in engineering applications demands continued advancement in measurement methods to fully understand physical processes, particularly in dense bubble flows. A method for reconstructing a dense three-dimensional bubble field was presented in this paper. The bubble field was induced by a turbulent plunging jet impinging on a free-surface. Synthetic aperture refocusing of images captured by multiple cameras allowed for generation of a focal stack. Bubbles appear in sharp focus on the slice of the stack corresponding to the true depth of the bubble, and appear blurred on other slices. An extraction algorithm enabled measurement of bubble size and location throughout the volume. The algorithm involved applying an attenuation function to retain regions with large gradients, followed by the generation of minimum images and the corresponding depth maps over depth windows. Potential features were labeled from an edge image of each minimum image, and sorted into large and small bubble classes. An ellipse detection algorithm [21] yielded geometric properties of large bubbles, while a thresholding and area based algorithm provided properties of small bubbles. The resulting size distributions and instantaneous location gives insight into the spatial distribution of various size bubbles in the flow. Ultimately, time-resolved bubble tracks can be generated from the data sets. The technique has ramifications for a variety of multiphase flow problems which demand instrumentation capable of measuring in dense fields.
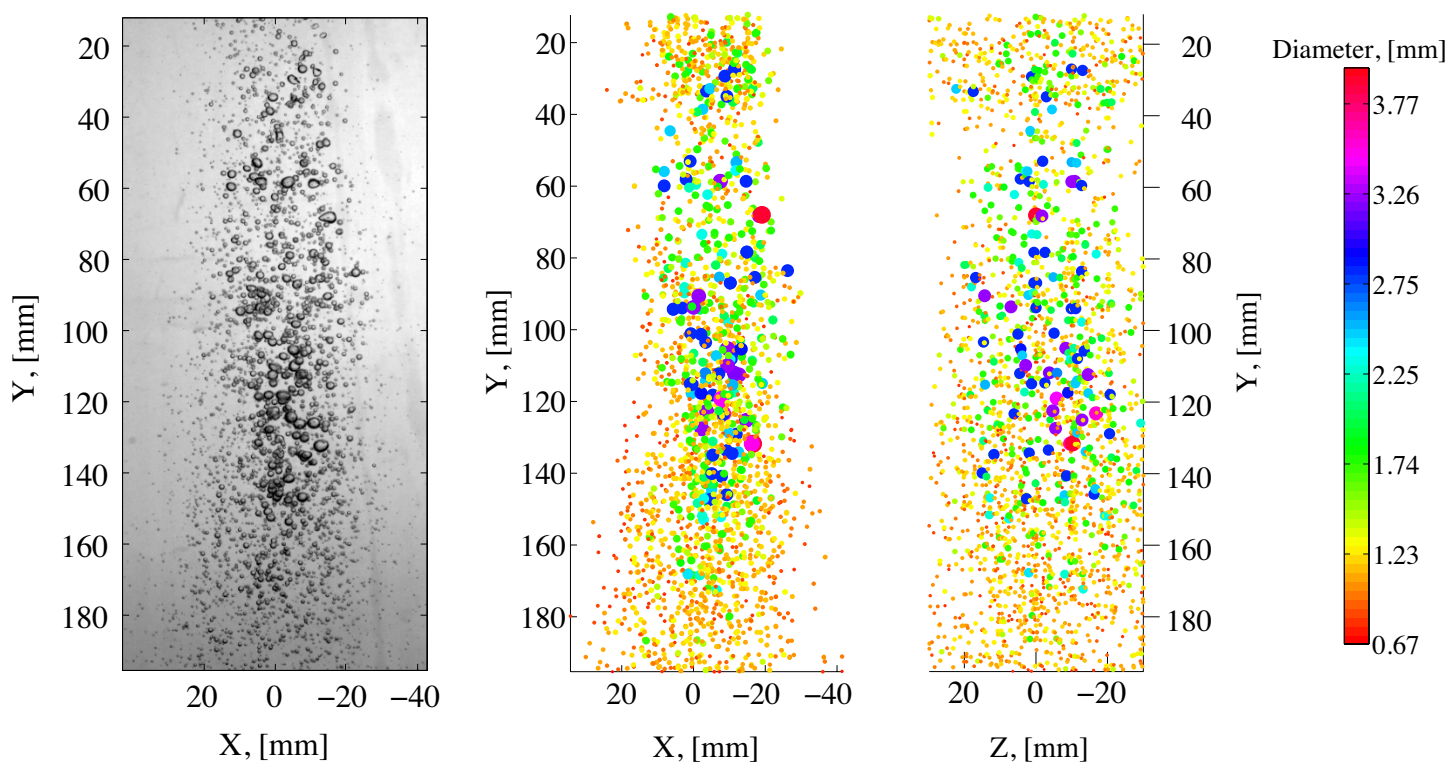
Copyright © 2011 by ASME

**FIGURE 10**: FROM LEFT TO RIGHT: RAW IMAGE FROM CENTER CAMERA OF THE ARRAY REPROJECTED ONTO THE $Z = 0$ mm FOCAL PLANE, $X - Y$ VIEW OF BUBBLE SIZE AND SPATIAL DISTRIBUTION, $Z - Y$ VIEW OF BUBBLE SIZE AND SPATIAL DISTRIBUTION, AND COLOR BAR CORRESPONDING TO THE TWO BUBBLE DISTRIBUTION PLOTS.

## REFERENCES

[1] Chanson, H., and Manasseh, R., 2003. "Air entrainment processes in a circular plunging jet: void-fraction and acoustic measurements". *Journal of Fluids Engineering,* *125*(5), September, pp. 910–921.

[2] Bröder, D., and Sommerfeld, M., 2007. "Planar shadow image velocimetry for the analysis of the hydrodynamics in bubbly flows". *Measurement Science and Technology,* *18*(8), July, p. 2513.

[3] Pereira, F., Gharib, M., Dabiri, D., and Modarress, D., 2000. "Defocusing digital particle image velocimetry: a 3-component 3-dimensional DPIV measurement technique. Application to bubbly flows". *Experiments in Fluids,* *29*(7), pp. S078–S084.

[4] Tian, L., Loomis, N., DomÌnguez-Caballero, J., and Barbastathis, G., 2010. "Quantitative measurement of size and three-dimensional position of fast-moving bubbles in air-water mixture flows using digital holography". *Appl. Opt.,* *49*(9), 03, pp. 1549–1554.

[5] Lin, T. J., and Donnelly, H. G., 1966. "Gas bubble entrainment by plunging laminar liquid jets". *AIChE,* *12*(3), pp. 563–571.

[6] Oguz, H. N., Prosperetti, A., and Lezzi, A. M., 1992. "Examples of air-entraining flows". *Physics of Fluids A: Fluid Dynamics,* *4*(4), pp. 649–651.

[7] Eggers, J., 2001. "Air entrainment through free-surface cusps". *Phys. Rev. Lett.,* *86*(19), May, pp. 4290–4293.

[8] Lorenceau, E., Quéré, D., and Eggers, J., 2004. "Air entrainment by a viscous jet plunging into a bath". *Phys. Rev. Lett.,* *93*(25), Dec, p. 254501.

[9] Reyssat, E., Lorenceau, E., Restagno, F., and Quéré, D., 2008. "Viscous jet drawing air into a bath". *Physics of Fluids,* *20*(9), p. 091107.

[10] Chanson, H., Aoki, S., and Hoque, A., 2006. "Bubble entrainment and dispersion in plunging jet flows: Freshwater vs. seawater". *Journal of Coastal Research,* *22*(3), June, pp. 664–677.

[11] Davoust, L., Achard, J. L., and El Hmmoumi, M., 2002. "Air entrainment by a plunging jet: the dynamical roughness concept and its estimation by a light absorption technique". *International Journal of Multiphase Flow,* *28*(9), August, pp. 1541–1564.

[12] Belden, J., Truscott, T. T., Axiak, M., and Techet, A. H., 2010. "Three-dimensional synthetic aperture particle im-

9

age velocimetry". *Measurement Science and Technology,* ***21***(12), December.

[13] Cheng, D.-c., and Burkhardt, H., 2005. "Template-based bubble identification and tracking in image sequences". *International Journal of Thermal Sciences,* ***45***(3), 3, pp. 321–330.

[14] Isaksen, A., McMillan, L., and Gortler, S. J., 2000. "Dynamically reparameterized light field". In SIGGRAPH '00: Proceedings of the 27th annual conference on Computer graphics and interactive techniques, ACM Press/Addison-Wesley Publishing Co., pp. 297–306.

[15] Vaish, V., Garg, G., Talvala, E., Antunez, E., Wilburn, B., Horowitz, M., and Levoy, M., 2005. "Synthetic aperture focusing using a shear-warp factorization of the viewing transform". In Proceedings of the 2005 IEEE Computer Society Conference on Computer Vision and Pattern Recognition (CVPR05') - Workshops, Vol. 3, IEEE Computer Society, p. 129.

[16] Elsinga, G., Scarano, F., Wieneke, B., and van Oudheusden, B., 2006. "Tomographic particle image velocimetry". *Experiments in Fluids,* ***41***(6), pp. 933–947.

[17] LaFoy, R. R., 2010. Personal Communication.

[18] Wieneke, B., 2008. "Volume self-calibration for 3D particle image velocimetry". *Experiments in Fluids,* ***45***, pp. 549–556.

[19] Scarano, F., and Poelma, C., 2009. "Three-dimensional vorticity patterns of cylinder wakes". *Experiments in Fluids,* ***47***(1), 07, pp. 69–83.

[20] Bongiovanni, C., Chevaillier, J. P., and Fabre, J., 1997. "Sizing of bubbles by incoherent imaging: defocus bias". *Experiments in Fluids,* ***23***(3), 07, pp. 209–216.

[21] Xie, Y., and Ji, Q., 2002. "A new efficient ellipse detection method". *Pattern Recognition, International Conference on,* ***2***, p. 20957.